Numerical investigation of soot formation from microgravity droplet combustion using heterogeneous chemistry

Alessandro Stagni*, Alberto Cuoci, Alessio Frassoldati, Eliseo Ranzi, Tiziano Faravelli

Department of Chemistry, Materials, and Chemical Engineering "G. Natta", Politecnico di Milano, Milano 20133, Italy

ABSTRACT

The use of isolated droplets as idealized systems is an established practice to get an insight on the physics of combustion, and an optimal test field to verify physical submodels. In this context, this work examines the dynamics of soot formation from the combustion of hydrocarbon liquid fuels in such conditions. A detailed, heterogeneous kinetic mechanism, describing aerosol and particle behavior through a discrete sectional approach is incorporated. The developed 1-dimensional model accounts for (i) non-luminous and luminous radiative heat losses, and (ii) incomplete thermal accommodation in the calculation of the thermophoretic flux. The combustion of droplets of *n*-heptane, i.e., the simplest representative species of real fuels, was investigated as test case; an upstream skeletal reduction of the kinetic mechanism was carried out to limit calculation times. After checking the performance of the reduced mechanism against gas-phase experimental data, the transient evolution of the system was analyzed through a comprehensive study, including fiber-suspended ($D_0 < 1$ mm) as well as free ($D_0 > 1$ mm) droplets.

The different steps of soot evolution were quantified, and localized in the region between the flame front and the soot shell, where particle velocity is directed inwards because of thermophoresis, and residence times are much higher than what usually found in diffusion flames. As a result, growth, coalescence, and aggregation steps are significantly enhanced, and soot accumulates in the inner shell, with an evident modification of the particle size distribution, if compared to what observed in conventional combustion conditions. The model exhibits a satisfactory agreement with experimental data on flame temperature and position around the droplet, while for larger droplets an increasing sensitivity to the radiation model was observed. It is found that the latter has a significant impact on the production of soot, while scarcely affecting the location of the soot shell. On the other side, the inclusion of incomplete thermal accommodation in the thermophoretic law brought about more accurate predictions of both volume fractions and shell location, and highlighted the primary role of thermophoresis in these conditions, as already found in literature through more simplified approaches.

© 2017 The Authors. Published by Elsevier Inc. on behalf of The Combustion Institute.
This is an open access article under the CC BY license. (http://creativecommons.org/licenses/by/4.0/)

1. Introduction

Nowadays, one of the major concerns raised by the combustion of liquid fuels is related to the formation of soot, toward which the interest of the scientific community is mostly motivated by its impacts on combustion efficiency [1], global warming [2,3], and human health [4–6]. Indeed, the use of a liquid feed in the form of a spray, and the resulting heterogeneous combustion create favorable conditions for particle nucleation from Polycyclic Aromatic Hydrocarbons (PAH) and their subsequent growth [7]. The significant amount of soot is the macroscopic outcome of the interaction

among several processes affecting real devices, including fuel evaporation and combustion, convection, and radiation. The timescale overlapping between the phenomena at stake results in the impossibility to decouple them, and makes the direct investigation of such systems a very challenging task.

In the attempt to gain a deeper understanding of the dynamics of droplet combustion and soot formation, as well as to develop and test submodels before their implementation in the Computational Fluid Dynamic (CFD) codes, in the latest decades significant experimental and modeling effort has been directed towards the combustion of simpler, idealized systems like spherical droplets in microgravity conditions [8–11]. Although their size is significantly larger than those found in real systems – millimeters instead of tens of microns – and they do not consider buoyancy-related effects, they provide fundamental information about the intricate

---

* Corresponding author.
  E-mail address: alessandro.stagni@polimi.it (A. Stagni).

Nomenclature

Roman Symbols

$\hat{h}_R$	Enthalpy of formation [J/kg]
c_p	Constant-pressure specific heat [J/kg/K]
dp	Soot primary particle diameter [m]
fv	Soot volume fraction [-]
I	Radiation intensity [W/m^2]
I_b	Blackbody intensity [W/m^2]
j	Flux [kg/m^2/s]
K	Burning rate [mm^2/s]
k	Thermal conductivity [W/(m·K)]
N_d	Soot number density [1/m^3]
q_R	Heat of radiation [W/(m^2·K)]
r_d	Droplet radius [mm]
v	Velocity [m/s]
$V_{th,r}$	Thermophoretic diffusivity [-]

coupling between the involved physical and chemical processes. As a matter of fact, they represent an optimal trade-off between the complexity of the problem, which is reduced to one spatial dimension because of spherical symmetry, and its comprehensiveness, since most phenomena involved in spray combustion are still considered, e.g. evaporation- and diffusion-induced transport, heterogeneous properties, radiation, and aerosol chemistry. In this way, the physical submodels representing each of them can be benchmarked in relatively "simplified" conditions. Conversely, assessing theoretical models of the governing phenomena from the interpretation of multidimensional experiments would be much more complicated, because of the resulting physical (and therefore, numerical) complexity.

For this reason, large experimental activity on soot formation in spherical droplets was carried out via reduced-gravity experiments. According to the droplet size, such conditions were attained either through drop towers or in the outer space. Most experimental campaigns date back to around 1990s: the shell-like structure of soot, placed between the flame layer and the droplet surface, was first observed by Shaw et al. [12]. The reason behind such a peculiarity was later attributed by Jackson and Avedisian [13] to the competition between the convective - or Stefan - flow, due to evaporation, and the thermophoretic flow acting on particles. They correlated the decrease in the burning rate with droplet size to soot production because of a combination of barrier and radiation effect, affecting the total heat transferred to the droplet. The structure of the flame enclosing the droplet was then studied by Mikami et al. [14] by using hooked thermocouples, and showing that the maximum temperature region, i.e. the reaction zone, is located outside of the yellow luminous zone, whose color is due to radiation from soot. The transient evolution of soot volume fractions was quantified in later works [15–17]: the maximum values were found to be between 10 and 100 ppm, i.e. more than one order of magnitude higher than what observed in gas-phase diffusion flames with the same fuels [18,19]. Finally, experiments on space laboratories [11,20,21] allowed an extensive investigation on large-sized droplets (super-millimetric), whose combustion dynamics cannot be followed in drop towers because of their insufficient length. In this way, light could be shed on radiative extinction of large droplets [20] and cool flame burning due to the low-temperature chemistry of *n*-alkanes [21,22].

From a modeling standpoint, a detailed description of the key phenomena affecting spherical droplet combustion is not straightforward, and it is often not compatible with an acceptable computational effort. The formation of soot adds substantial complexity to the modeling of droplet dynamics, which has been the sub-

ject of extensive research for long time [23–26]. First of all, the transient evolution of soot is strongly correlated to the gas-phase chemistry, from which soot precursors (PAH) are generated. Therefore, a detailed kinetic description is a necessary requirement to be predictive on soot formation. Second, the presence of soot has an impact on heat transfer and especially on luminous radiation, which on turn affects the burning rates and the overall combustion process. As a result, modeling activity has often been based on one or more assumptions to simplify the size of the problem and make it computationally viable: Chang and Shier [27] used a one-step reaction mechanism to parametrically study the correlation between soot production, flame radiance and droplet burning rates. Similarly, Baek et al. [28] analyzed soot/radiation interaction through global chemistry and a simplified two-equation model [29] describing the evolution of soot volume fraction and number density. On the other side, Jackson and Avedisian [30] were among the first to incorporate detailed chemistry in droplet calculations: coherently with experimental observations, they could find an increase in acetylene concentration (a key species among soot precursors) with the droplet diameter, but they could not analyze PAH evolution into soot particles because the adopted kinetic model described only gas-phase combustion. Later studies using detailed chemistry [8,31] neglected soot formation and the related effects on the combustion behavior.

In the light of the previous modeling efforts, in this work the dynamics of soot formation in the combustion of spherical droplets is investigated through a comprehensive approach, which incorporates a detailed kinetic mechanism representing soot formation from the underlying gas-phase. An existing mathematical model of droplet evaporation and ignition is extended towards a detailed description of the key processes involving soot: besides the description of aerosol dynamics coupled to gas-phase kinetics, nongray radiation effects are considered for both gas-phase species and solid particles, and thermophoretic effect on solid particles is accounted for. The main features of the mathematical model are recalled in Section 2, with an emphasis on the submodels of major relevance for the purposes of this work. The development of the kinetic mechanism of soot formation is then separately outlined in Section 3. In Section 4, the model is leveraged to shed light on the transient evolution of the two-phase system, and the role of soot in such dynamics: numerical predictions are compared against the experimental data collected so far, and *n*-heptane is used as case study since it has been the most studied fuel in microgravity conditions. Conclusions are drawn in Section 5.

2. Mathematical model

The mathematical model describes the combustion of an isolated droplet in a gas-phase environment, idealizing the experimental conditions of drop towers and outer space. The core framework is fully described in [32,33] and is based on the following assumptions:

- Spherical symmetry and absence of gravity;
- Constant pressure;
- Absence of reactions in liquid phase;
- Thermodynamic equilibrium at the liquid/gas interface.

In particular, spherical symmetry allows to consider the problem as 1-dimensional. Considering a monocomponent fuel, the conservation equations for energy and velocity in the liquid phase are:

$$\rho_L c_{p,L}\left(\frac{\partial T_L}{\partial t} + v_L \frac{\partial T_L}{\partial r}\right) = \frac{1}{r^2}\frac{\partial}{\partial r}\left(r^2 k_L \frac{\partial T_L}{\partial r}\right) \tag{1}$$

$$\frac{\partial \rho_L}{\partial t} + \frac{1}{r^2}\frac{\partial}{\partial r}\left(r^2 \rho_L v_L\right) = 0 \tag{2}$$

where the subscript L denotes the liquid phase. ρ is the density, v the convective velocity, c_p the constant-pressure specific heat of the fuel and k the thermal conductivity. The dependence of ρ_L, $c_{p,L}$ and k_L on temperature is described through the correlations found in the Yaws' database [34,35]. Symmetry conditions are imposed in the center of the droplet. Similar equations are obtained for the gas phase, although further contributions must be included:

$$\rho_G\left(\frac{\partial Y_{G,i}}{\partial t} + v_G\frac{\partial Y_{G,i}}{\partial r}\right) = -\frac{1}{r^2}\frac{\partial}{\partial r}\left(r^2\left(j_{diff,i} + j_{th,i} + j_{soret,i}\right)\right) + \dot{\Omega}_{G,i}$$
$$i = 1\ldots NS \tag{3}$$

$$\rho_G c_{p,G}\left(\frac{\partial T_G}{\partial t} + v_G\frac{\partial T_G}{\partial r}\right) = \frac{1}{r^2}\frac{\partial}{\partial r}\left(r^2 k_G\frac{\partial T_G}{\partial r}\right)$$
$$- \sum_i j_{diff,i}c_{p,G,i}\frac{\partial T_G}{\partial r} - \sum_{i=1}^{NS}\dot{\Omega}_{G,i}\hat{h}_{R,i} - \nabla q_R \tag{4}$$

$$\frac{\partial \rho_G}{\partial t} + \frac{1}{r^2}\frac{\partial}{\partial r}\left(r^2 \rho_G v_G\right) = 0 \tag{5}$$

where the subscript G indicates gas-phase properties. Considering the ith gas-phase species, Y_i is its mass fraction, $j_{diff,i}$ is its gas-phase diffusion flux evaluated through the Fick's law, $j_{th,i}$ is its flux due to thermophoresis (cfr. Section 2.2), $j_{soret,i}$ is its flux generated by Soret effect, $\dot{\Omega}_i$ is its formation rate: $\dot{\Omega}_i = \sum_{j=1}^{NR}\nu_{ij}r_j$, with r_j being the rate of the jth reaction (NS and NR are respectively the total number of species and reactions). $\hat{h}_{R,i}$ is the mass enthalpy of formation of the ith species and finally q_R is the radiative heat flux (cfr. Section 2.1). Diffusiophoretic and photophoretic effects are here neglected, although a minor influence on soot formation had been hypothesized in previous works [36,37].

Liquid/gas interface properties are evaluated by imposing flux continuity of mass and energy, and by imposing thermodynamic equilibrium for species. Considering the low-pressure conditions investigated here, the use of Raoult's law can be considered as acceptable. At the outer boundary (around 80–100 times the droplet radius), Dirichlet conditions are imposed for species and temperature. The droplet is ignited by simulating a numerical spark: in the proximity of the liquid interface, a temperature profile peaking at 2000 K is imposed as initial condition. Although in experimental devices the spark might in principle compromise the spherical symmetry, this effect is neglected in this model, as already done in previous works [32,38].

2.1. Radiation

The gas-phase energy balance (4) takes into account the radiation contributions from non-luminous gases (CO_2/H_2O) and luminous soot particles via the divergence of the radiative heat flux ∇q_R. Considering a gray medium, the radiative energy balance is evaluated as [39]:

$$\nabla q_R = \kappa\left(4\pi I_b - \int_{4\pi} I d\Omega\right) \tag{6}$$

where κ is the Planck mean absorption coefficient, I_b is the blackbody intensity $I_b = \sigma T^4/\pi$ (σ is the Stefan–Boltzmann constant) and I is the radiation intensity. Different approaches exist to model I: here, the P-1 radiation model was adopted, i.e. the first-order approximation of I into a series of spherical harmonics. Alternatively, the Discrete Ordinates Model (DOM) was successfully used in previous works on microgravity droplets [28,38], but P-1 approximation allows a more significant ease of the computational load, without an excessive loss in accuracy if radiative intensity is near-isotropic [39].

A comparison between radiation models is beyond the scope of this work. Rather, considering the investigated problem, a more critical aspect is constituted by the representation of the medium absorptivity, due to the nongray behavior of water and carbon dioxide, and to the major role of soot radiation. A convenient way to represent a nongray medium consists in using a Weighted-Sum-of-Gray-Gases Model (WSGGM) [40]. With this methodology, a number of equivalent gray gases are used for each medium, weighted through temperature-dependant factors. These are obtained via fitting procedures with experimental measurements:

$$\omega_k = \sum_{j=1}^{J} b_{k,j}T^{j-1} \tag{7}$$

The combination between $N_g + 1$ and N_s equivalent gray gases (for absorbing gases and soot, respectively) produces $(N_g + 1) \times N_s$ total gray gases. Indeed, a transparent window must be considered for CO_2/H_2O, i.e. $\kappa_{g,0} = 0$. For each (n,m) gray gas the combined absorption coefficient can be evaluated as:

$$\kappa_{n,m} = \kappa_{s,n} + P\kappa_{g,m} \tag{8}$$

where P is the pressure. The combined (n,m) weighting factor is obtained through the product of the weighting factors:

$$\omega_{n,m} = \omega_n \cdot \omega_m \tag{9}$$

Once the coefficients have been calculated, one equation (6) is solved for each gray gas [28,40]:

$$\nabla q_{R,n,m} = \kappa_{n,m}\left(4\pi \omega_{n,m}I_b - \int_{4\pi} I_{n,m}d\Omega\right) \tag{10}$$

then summing up the respective contributions to obtain ∇q_R. A critical point in the development of WSGG models consists in the parameters estimation for the equivalent gray gases: usually, this is done through fitting procedures [41,42] for mixtures with fixed H_2O/CO_2 ratios, and separately for soot [43]. Recently, Cassol et al. [44] developed a novel procedure to estimate coefficients for arbitrary compositions of H_2O, CO_2 and soot. Starting from individual species correlations and related equivalent gray gases, they extended the combination procedure to evaluate the combined absorption coefficient and weighting factor (Eq. (8) and (9)):

$$\kappa_{m,j_m} = \kappa_{H_2O,j_{H_2O}} + \kappa_{CO_2,j_{CO_2}} + \kappa_{s,j_s} \tag{11}$$

$$\omega_{m,j_m} = \omega_{H_2O,j_{H_2O}} \cdot \omega_{CO_2,j_{CO_2}} \cdot \omega_{s,j_s} \tag{12}$$

Starting from 4 gray gases for H_2O, CO_2, and soot, respectively, 100 mixture gray gases are obtained, whose radiative contribution is calculated through Eq. (10). Considering the time- and space-variable composition of the gas-phase environment, Cassol model is thus able to guarantee the needed flexibility in managing the radiative contribution to the energy balance (4), without compromising computational efficiency. Therefore, it is used as reference model for the purposes of this work.

2.2. Thermophoretic flux

The key role of thermophoretic force in trapping soot particles within the flame, then allowing their significant growth, had been already hypothesized by Jackson et al. [45] after experimental observations. However, a complete understanding and accurate quantification of this effect has not been obtained so far. In qualitative terms, the thermophoretic force is due to the difference in the momentum of gaseous molecules colliding with solid particles, due to temperature gradient. It results in solid particles being subject to a force in the opposite direction to the temperature gradient. In

quantitative terms, all the theories describing thermophoretic velocity can be reduced to the general expression [46]:

$$v_{th} = -V_{th,r} \frac{\mu_G}{\rho_G} \frac{\nabla T}{T_G} \tag{13}$$

where μ is dynamic viscosity, T is temperature, and $V_{th,r}$ is the thermophoretic diffusivity (or reduced thermophoretic velocity). This depends on three main parameters:

1. The Knudsen number Kn, i.e. the ratio between the gas free mean path and the characteristic size of the particle, thus determining whether collisions occur in a free-molecular ($Kn \gg 1$), slip-flow ($Kn \ll 1$) or transition ($Kn \approx 1$) regime;
2. The ratio Λ between thermal conductivities of gas and particles.
3. The momentum and thermal accommodation factors α_m and α_T, which account for the type of collision between gas and particles. The limit values of 0 and 1 respectively correspond to specular and diffuse reflection.

Considering spherical particles, several theoretical expressions for $V_{th, r}$ have been independently derived, and the review by Sagot [47] compares their predictions with experimental measurements. If $Kn \gg 1$, i.e. in the free molecular regime, and with the hypothesis of perfect accommodation ($\alpha_T = \alpha_m = 1$) and $\Lambda \ll 1$ all the theories converge to the formulation obtained by Waldmann and Schmitt [48], i.e. $V_{th,r} \approx 0.538$. Although $Kn \ll 1$ for larger particles, experimental measurements [49] and theoretical research [50] showed that, as far as soot particles are concerned, thermophoretic velocities scarcely depend on their dimensions, but rather depend on primary particle sizes because of the open structure of the aggregates.

Moreover, although at low temperatures ($T \leq 500\,K$) α_T is usually equal to 1, at higher temperatures like those occurring during combustion, an incomplete thermal accommodation can be expected [51]. Snelling et al. [52] reported significant uncertainty on such parameter, estimated to be around 15%: in their experiments, carried out in a laminar coflow diffusion flame fed by ethylene, they developed a model able to estimate α_T from the mean primary particle size d_p. Considering a measured value of $d_p = 29\,nm$ they found a value of $\alpha_T = 0.37$, coherent with the available literature data (ranging from 0.26 to 0.90). On the other side, using the $d_p = 38\,nm$ measured by Manzello and Choi [53] in microgravity droplet flames α_T becomes equal to 0.54.

The possibility of an incomplete thermal accommodation is included in some theoretical formulations of $V_{th, r}$ [51,54]. The application of the model proposed by Beresnev and Chernyak [54,55], assuming a free-molecular regime, with $\alpha_T = 0.54$, $\Lambda = 0.1$ and $\alpha_m = 1$ returns $V_{th,r} = 0.654$. Similarly, the model of Talbot et al. [51], which extends the base formulation of Waldmann to the possibility of incomplete thermal accommodation, returns $V_{th,r} = 0.660$, comparable to the previous one. The capability of the model by Beresnev and Chernyak in predicting the influence of α_T on thermophoretic velocity was extensively verified by Sagot [47]. Thus, the obtained value of $V_{th,r}$ will be used for the purposes of this work.

3. Kinetic mechanism of soot formation

The overall kinetic mechanism was derived from the POLIMI model [56] describing the pyrolysis and oxidation of a variety of hydrocarbon fuels: the hierarchy and modularity features behind its formulation allow to easily obtain the low- and high-temperature combustion mechanism including Primary Reference Fuels (PRF), PAHs and real fuels. The 1412 version of such model accounts for 352 species and 13264 reactions, and its performance has been widely verified in several works [57–59]. In or-

der to describe the soot dynamics, gas phase chemistry is coupled to soot chemistry through the discrete sectional approach recently developed by Saggese et al. [60]. Such methodology represents the aerosol distribution through a 2-dimensional discretization into pseudo- or lumped-species, called BINs, representing a class of particles with defined molecular mass (defined by a number index $k = 1 \ldots 20$) and H/C ratio (indicated by a letter A, B, C in descending H/C order). On turn, BINs are split into three categories: heavy PAHs (MW $\leq 3,000\,g/mol$), soot particles ($3,000\,g/mol < MW \leq 500,000\,g/mol$) and soot aggregates (MW $> 500,000\,g/mol$). The selection of the size of the first primary particle (320 carbon atoms, i.e. an atomic mass of about 4000 amu) was chosen after the experimental observations of the heavy PAHs obtained from flame-generated soot [61–64], and is in agreement with the particle sizes measured by Bladh et al. [65]. On the other side, the dimensions of the first aggregate (around 80,000 carbon atoms, i.e. an atomic mass of about 10^6 amu and a collision diameter of approx. 13.7 nm) were chosen after the experimental measurements by Zhao et al. [66] on the mobility diameter of aggregates. Particles differ from aggregates because of their postulated spherical shape. Conversely, aggregates are considered as mass fractals, with a fractal dimension assumed as equal to 1.8. This value is in general agreement with the experimental measurements carried out for nascent soot in premixed ethylene flames [67] and for rich sooting flames [68].

Similarly to what done with the gas-phase, soot model was conceived following a reaction-class approach, where the newly introduced classes involve both gas-phase species and solid-phase pseudo-species. The reaction rates of the different classes are obtained through analogy with similar reactions [60], already present in the gas-phase model. Doing so, the coupled system can be described in a pseudo-homogeneous way, and the resulting kinetic input is still compatible with the standard CHEMKIN format. The resulting, high-temperature scheme includes 297 species among 16797 reactions; on the other side, the low- and high-temperature scheme accounts for 426 species among 20145 reactions.

3.1. Skeletal reduction

The high level of detail on the description of soot obtained with this methodology results in a mechanism size particularly demanding, even for 1D applications. For this reason, a skeletal reduction was carried out, such to make calculations more viable. Nevertheless, implementing a skeletal reduction methodology for a mechanism including soot formation is not straightforward, and must consider three main issues, if compared to a classic gas-phase mechanism:

- The time scales of soot formation, growth and oxidation are orders of magnitude longer than ignition time [69]. Therefore, preserving ignition delay time is a necessary, but not sufficient condition to retain accuracy on soot dynamics, and ignition-targeted reduction methodologies [70,71] would fail when soot is the actual reduction target.
- When targeting the skeletal reduction process at soot formation, its continuous distribution and the consequent modeling into pseudo-species (BINs) require a different strategy and different targets to address the whole reduction procedure.
- Soot formation competes with its oxidation, which occurs at fuel/air ratios close to stoichiometric, when particles move away from the rich zone. In such conditions, soot oxidation mostly occurs by means of OH and O_2 [72]. This cannot be observed in the 0D systems typically used for mechanism reduction, due to the total consumption of oxygen after fuel oxidation in rich conditions.

Table 1

Operating conditions used for the skeletal reduction of the soot mechanism.

	Range
Temperature	600 K-1800 K
Pressure	1 atm
Equivalence ratio	0.5-4

To address these points, the methodology described in [73], known as Species-Targeted Sensitivity Analysis was extended to include specific soot properties, since every BIN represents only a discrete portion of the continuous particle distribution constituting soot. In macroscopic terms, 3 properties usually characterize the soot aerosol: (i) volume fraction f_v, (ii) number density N_d and (iii) Particle Size Distribution Function (PSDF). They are not independent from each other, because N_d can be obtained by integrating PSDF, and f_v can be obtained by combining mass fractions and particle density. Therefore, by considering isothermal reaction states in 0D batch reactors, sampled in the range indicated in Table 1, two targets were selected to constrain sensitivity analysis and species selection:

1. Soot mass fraction profile over time in a 0D reactor;
2. Soot PSDF, at the time where its mass fraction is maximum;

With the same procedure described in [73], the importance of each species constituting the complete mechanism is done by evaluating the error in terms of distance – ε_D – and similarity – ε_S – between the original mechanism and the one without the analyzed species. Moreover, to keep into account oxidation pathways after particle transport, the outlet products coming from the first reactor enter a second one with identical operating conditions, with oxygen fed in parallel at stoichiometric conditions. Oxidation dynamics is reconstructed through soot mass fraction profile and the error following the removal of each species is calculated again through ε_D and ε_S. The whole process is outlined in Fig. 1.

Overall, 6 error indices are obtained, 2 per each of the three curves. They are combined following the statistical procedure illustrated in [73], such that a univocal ranking is obtained. Fol-
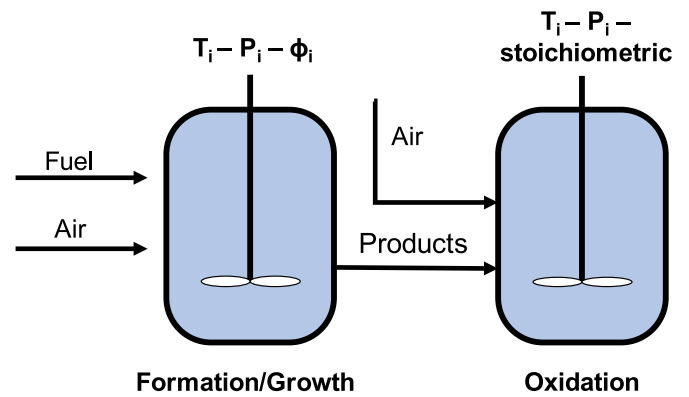

Fig. 1. Double-reactor configuration adopted for the reduction of soot mechanism (cfr. [84]).

Table 2

Threshold values and sizes of the two soot mechanisms obtained via Soot-Targeted Sensitivity Analysis.

Mechanism	ε_D	ε_S	Original mechanism		Reduced mechanism	
			Species	Reactions	Species	Reactions
HT	0.15	0.06	297	16,797	201	8690
LT+HT			426	20,145	227	9461

lowing the obtained *Soot-Targeted Sensitivity Analysis*, the mechanisms listed in Table 2 were obtained for soot formation from *n*-heptane combustion, respectively for high-temperature (HT) and low- (LT) and high-temperature conditions. It is worth highlighting that 79 BINs (48 molecules + 31 radicals) were retained out of the original 100 (50 species + 50 radicals). Most of the removed ones are gas-phase compounds: considering that the sectional model is conceived in such a way that every BIN has a double mass than the previous one, removing an intermediate section would break the growth chain via coalescence or aggregation, and their growth could continue only via coalescence/aggregation with the smaller ones, having a lower mass. Also, it is important to note that most of the removed BINs belong to the class with the highest H/C ratio
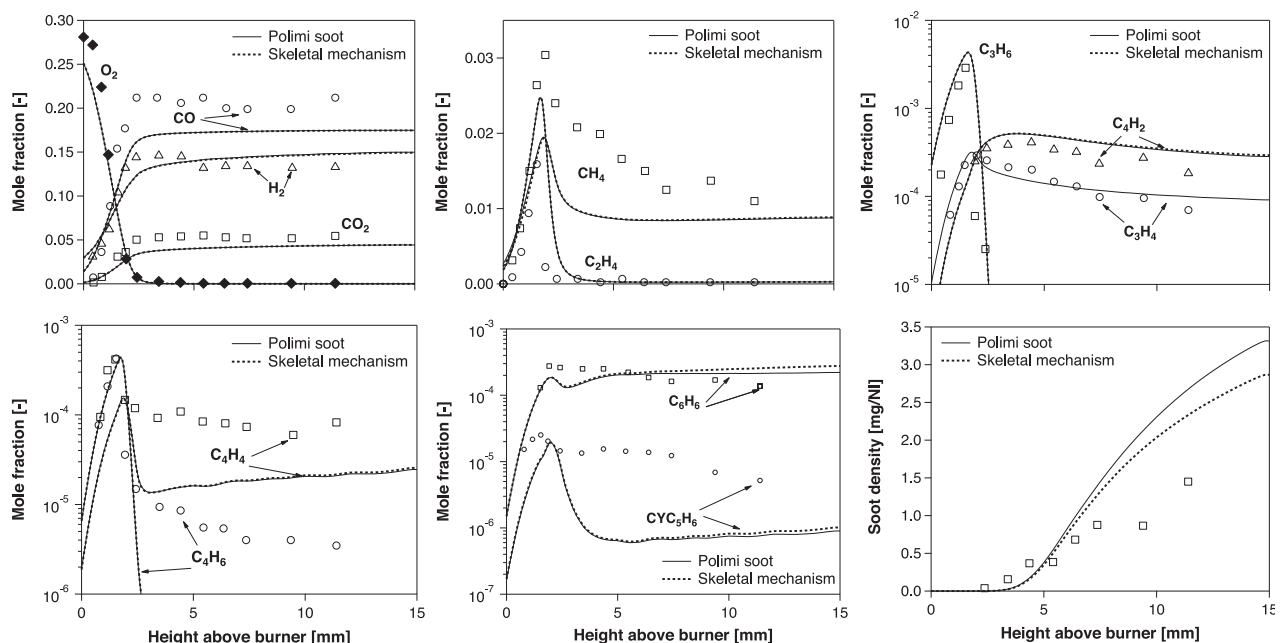

Fig. 2. Numerical predictions of flame speciation and soot formation in a *n*-heptane/air laminar premixed flame. C/O = 0.70. Experimental data from [77].
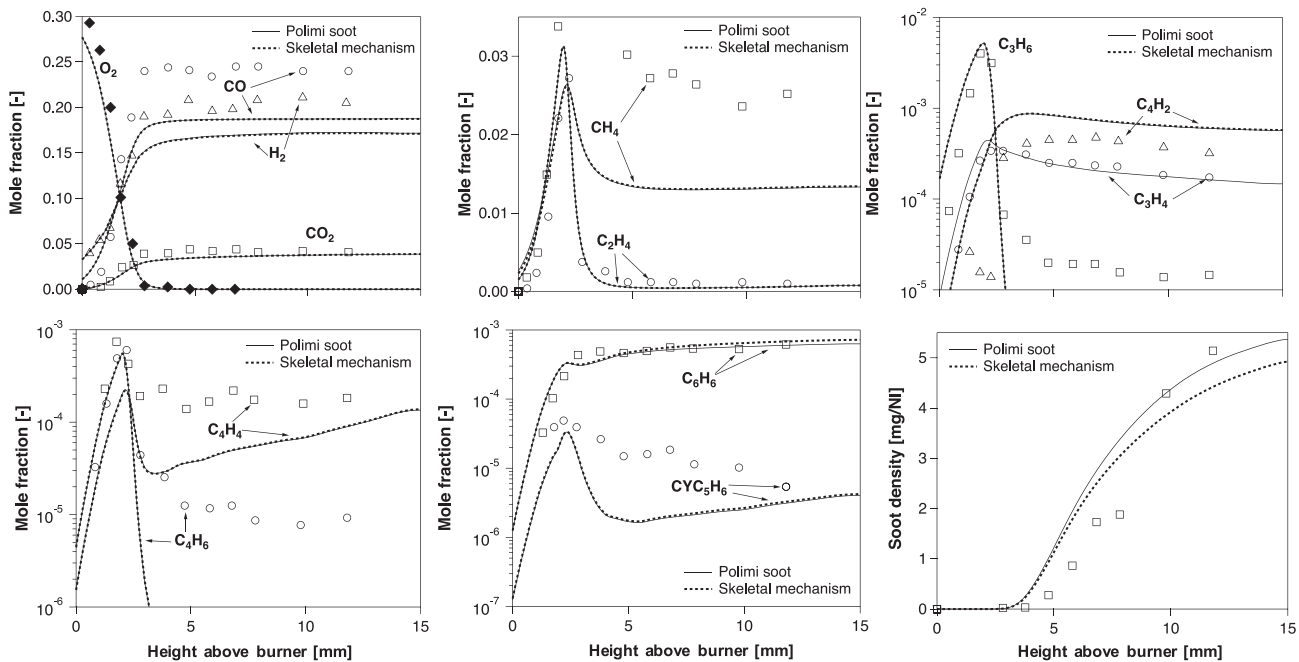
Fig. 3. Numerical predictions of flame speciation and soot formation in a *n*-heptane/air laminar premixed flame. C/O = 0.80 Experimental data from [77].

("A" class): this indicates that in the considered conditions dehydrogenation plays a major role, to the extent that "A" class BINs disappear before reaching their larger sizes.

Considering that the computational time scales, at worst, with the third power of the number of species in the problems governed by the factorization of the Jacobian, adding this upstream skeletal reduction allowed to decrease the simulation times by a factor 2.5 – 3, as verified *a posteriori* in sample benchmarks.

3.2. Mechanism benchmark

The performance of the complete model of soot formation was already verified in the reference paper [60]. Here, the skeletal mechanism is benchmarked against the original model and experimental data. Previous works have experimentally characterized PAH [74] and soot formation [75–77] from *n*-heptane in laminar flames. D'Anna et al. [77] analyzed laminar flame speciation in slightly sooting (C/O = 0.70) and heavily sooting (C/O = 0.80) conditions, and quantified the formation of major species, intermediates, PAH, and soot density. Based on both experimental concentrations, numerical predictions were obtained by using detailed [60] and skeletal mechanism in order to check the accuracy of the latter. The temperature profile was taken from experimental measurements, thus decoupling the energy balance: the heat losses of the burner depend on the experimental devices, and the flame cannot be considered as adiabatic. Results are shown in Figs. 2 and 3, and highlight two main aspects: on one hand, a reasonable agreement is observed for major species as well as some intermediates. A more significant deviation is observed for methane (CH_4), butadiene (C_4H_6), propylene (C_3H_6) and cyclopentadiene (CYC_5H_6). On the other side, benzene evolution is predicted very well, and the soot density profile is in substantial agreement with experimental measurements, also considering the uncertainty behind them [7,78]. Moreover, detailed and skeletal mechanism are overlapped as far as major species and small hydrocarbons are concerned; instead, the deviations of soot and its precursors are of the order of 15–20% at the burner outlet, in line with the accuracy targets of the reduction procedure (Table 2).
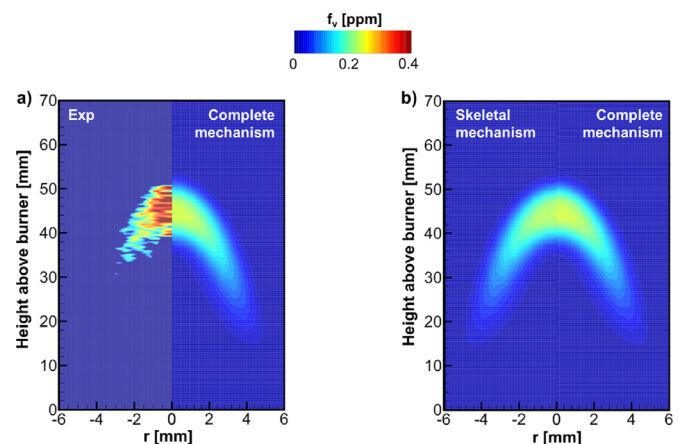

Fig. 4. Comparison between measured and simulated soot volume fraction fields. (a) Experimental (left) vs numerical (right) results, obtained via the Polimi soot mechanism; (b) Numerical results, as obtained with skeletal mechanism (left) and Polimi soot mechanism (right). Experimental data from [19].

Recently, the sooting propensity of gasoline surrogates and PRFs in coflow diffusion flames was considered by Kashif et al. [18,19]. The predictive capability of the kinetic mechanism in these conditions is of primary importance: here, the amounts of soot are generally higher than premixed flames because of the locally rich composition on the fuel side. Moreover, particle transport outside the reaction zone makes their oxidation possible, which competes with their formation and results in the final wedge-shaped profile observed in these conditions. The axisymmetric coflow burner used for such experiments was simulated via the `laminarSMOKE` software [79]. The inlet fuel mixture consisted of a carrier gas (equimolar CH_4/N_2), and the experiment was performed with two different molar fractions of *n*-heptane. Figure 4 shows the results related to the richer mixture ($X_{C_7H_{16}} = 0.0247$). Apparently, the shape of soot profiles is comparable between measurements and predictions. In absolute terms, soot volume fraction is underpredicted by a factor 2 along the axis of symmetry, but considering
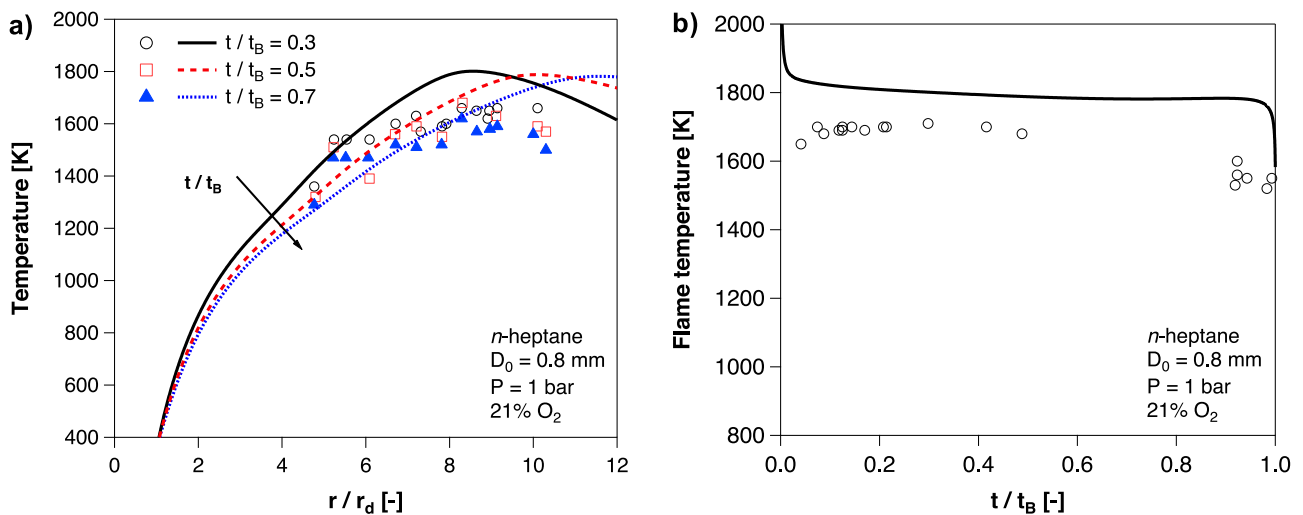
Fig. 5. Flame evolution over time in a *n*-heptane droplet ($D_0 = 0.8$ mm), burning in air at atmospheric pressure: experimental data [14] vs numerical predictions. (a) Radial temperature profile at different time steps. (b) Maximum flame temperature over time. t_B = total burning time of the droplet. r_d = droplet radius.
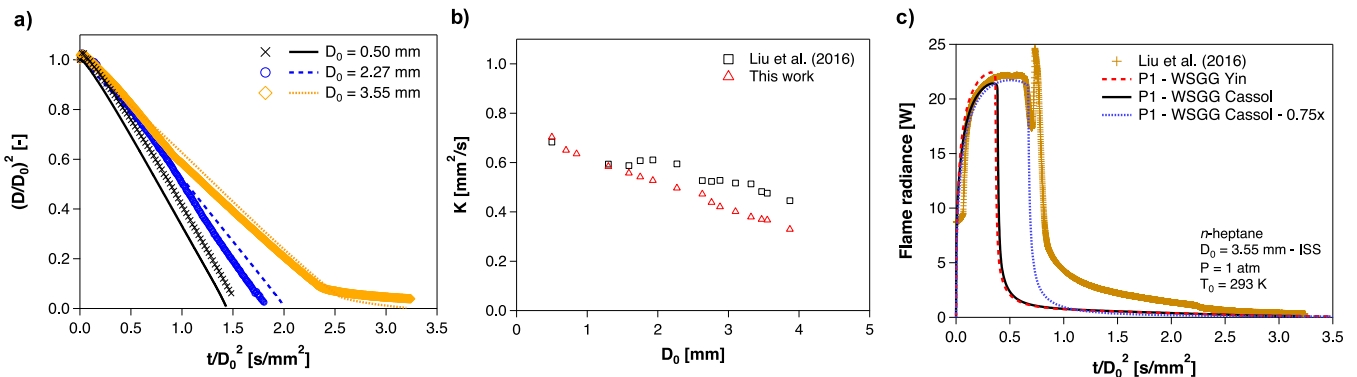

Fig. 6. Combustion of *n*-heptane droplets: (a) Time evolution of scaled diameter. (b) Dependence of K on initial diameter. (c) Comparison between measured wideband flame radiance and predicted radiance ($d_0 = 3.55$ mm). Experimental data from [21].

the very low volume fractions involved and the observed noise in experimental data, the overall agreement is still satisfactory. Above all, to the purposes of this work it is important to highlight that the skeletal reduction process does not bring about any loss of accuracy in soot volume fractions (Fig. 4b), and in spite of the added complexity of the 2-dimensional case, f_v fields predicted with the detailed and the skeletal mechanism are virtually overlapped.

4. Soot formation in the combustion of *n*-heptane droplets

The combustion of *n*-alkane droplets in microgravity conditions has been matter of comprehensive experimental campaigns in the latest decades. Therefore, enough data are available to support and benchmark the validity of the methodology proposed in this work. Considering *n*-heptane as test case, the transient droplet combustion was investigated in different conditions. An adaptive grid was used, with four different stretching factors: higher refinement was set in the region where flame and soot shell are expectably located, while a more coarse spacing was set in the far field. The single simulations required, on average, 8–10 hours for completion. In the following, the core of the numerical model is first briefly validated, through the analysis of flame structure and droplet burning rate. Later, the focus is set on soot dynamics in the considered systems.

4.1. Model validation

From the experimental side, understanding the transient flame evolution in a sooting droplet is not straightforward. The forma-

tion of soot around it prevents any invasive measurement in the inner part, since the thermocouple would be coated by soot, thus compromising the accuracy of results. Instead, insights can be provided on the outer part, where the use of proper coating of thermocouples to avoid catalytic effect can produce reliable data. Mikami et al. [14] studied the transient flame structure, by using hooked thermocouples, concentric with droplet size, to measure the outer temperature profile at different times. The case of combustion in air, at atmospheric pressure, is used here as reference for model benchmark. Figure 5 shows that the model is able to reproduce the shape of the radial temperature profile. An overestimation of the outer part of the temperature profile (Fig. 5a), and of its peak (Fig. 5b) can be observed; yet, as pointed out by Mikami and coworkers, the experimental measurements need correction because of radiative heat loss from thermocouple, such that the corrected flame temperature, for $0.3 \leq t/t_B \leq 0.6$, has been reported as 1782 K, i.e. in very good agreement with the numerical predictions. Figure 5a also shows that the unsteady burning conditions result in the flame front progressively moving away from the droplet surface, although the uncertainty of the reported measurements is too high to observe such behavior also in the experimental profiles; in order to observe this trend, a detailed description of the transient evolution is needed, and simplified analyses considering quasi-steady state conditions, or constant thermal and physical properties might provide approximate predictions.

As a matter of fact, the flame temperature has a critical impact on burning rates as well as the formation of soot itself, because of the temperature-dependent kinetic rates. Experimental evidence

[17,21,45] and numerical theories [21,38,80] show that the burning rate :

$$K = \left| \frac{d(D/D_0)^2}{d(t/D_0^2)} \right| \tag{14}$$

progressively decreases as D_0 increases, and that beyond a critical initial diameter, extinction is reached during combustion. By increasing the starting diameter, radiative losses assume a higher weight in the energy balance, since they roughly scale with D_0^3 [81]. As a result, the flame temperature gradually decreases, until combustion is no longer able to self-sustain. Therefore, an accurate representation of radiation is a necessary requirement to correctly describe the droplet burning rates as a function of D_0.

Liu et al. [21] analyzed, through an experimental campaign on different fuels complemented by a theoretical scale analysis, the effect of initial diameter on droplet combustion. The dependence of burning rate on initial diameter was numerically reproduced in the range $D_0 = 0.5 – 3.87$ mm, and Fig. 6 shows the key results of such analysis. The HT skeletal mechanism was used for the sub-millimetric simulations, since no extinction and subsequent low-temperature combustion is involved, whereas the LT+HT skeletal mechanism was used in the super-millimetric cases. At low initial diameters (i.e. ground-based experiments), K is in very good agreement with experimental data. On the other side, the decrease of K for larger droplets deserves a more specific attention. Figure 6b shows that the predicted burning rates decrease faster than the observed ones, and hot flame extinction is thus underestimated. Indeed, although the numerical model proved capable to estimate the overall flame radiance (Fig. 6c), the extinction diameter is very sensitive to the radiation model. The use of alternative WSGG fitting coefficients like those proposed by Yin [42] provides a comparable early extinction, and only an empirical correction to the radiation contribution in Eq. (8) (a factor 0.75) would result in a more accurate estimation of the extinction time. A more thorough analysis of the role of radiation in the hot- and low-temperature-extinction of isolated droplets is outside the scope of this work, and it was specifically investigated in previous studies [38,82]. For the present purposes, the use of a model able to take into account radiation from soot, like WSGG as proposed by Cassol et al. [44] assumes a higher importance, and is also an optimal tradeoff between the quality of results and the computational cost of the simulations.

The satisfactory predictions of the model are confirmed by the evolution of the Flame Standoff Ratio (FSR), i.e. the relative position of the flame front with respect to the droplet, normalized by the instantaneous diameter. As shown in Fig. 5a, the flame front cannot be considered as stationary. The accuracy in such prediction is an important index of model performance, in a parallel way to what flame speed represents in 1-dimensional laminar flames: it groups in a single value the effect of the droplet burning rate (and resulting convective velocity), gas-phase diffusivity, thermodynamic and kinetic properties. Figure 7 shows FSR evolution over time in two different experimental campaigns. In both cases, numerical predictions show FSR progressively increasing over time, also scaling with D_0^2. In the case of the data by Jackson and Avedisian (Fig. 7a), a constant offset can be observed between predictions and measurements: this is most likely due to the procedure to measure the flame front. In fact, the methodology adopted by the authors consisted in evaluating the average location of the yellow luminous shell around the droplet, whereas numerically FSR is usually evaluated as the location where the maximum temperature is reached. The yellow color is mostly due to radiation from soot, taking place as long as it is in high-temperature regions. There is negligible soot around the temperature peak, therefore the experimental procedure finds a lower FSR profile. On the other hand,

in the work of Liu et al. (Fig. 7b) the flame diameter was evaluated as the outer boundary of the blue zone surrounding the yellow central core. In this case, a consistent agreement between model and experimental data is observed. While no monotonic correlation appears between D_0 and FSR in the measurements, the model predicts a more detached flame with smaller diameters in the first part of combustion. This is due to the radiative heat losses, which increase with D_0 and then restrain the flame development, as it can be seen in Fig. 8. Finally, it is worthwhile noting that the flame extinction is also well predicted, as FSR significantly increases when the droplet diameter approaches zero.

4.2. Soot dynamics

The availability of a detailed model is of critical importance when the formation of soot is investigated. In this context, unsteady effects are critical in determining the evolution of the soot shell around the burning droplets. Its presence in significant amounts might affect droplet combustion because of its radiative power, with a strong coupling between gas and aerosol phase and an overall decrease of burning efficiency. In microgravity droplets, significantly higher amounts of formed soot are usually observed: even tens of ppm are locally produced by not heavily sooting fuels like *n*-heptane, which usually do not form soot volume fractions higher than 1 ppm (cfr. Figs. 2, 3 and 4).

The formation of soot particles is controlled by chemical kinetics, because of the relatively longer time scales, compared to ignition. In these specific conditions, two main peculiarities emphasize the role of soot kinetics: (i) the high gradients of fuel concentration over the radial coordinate, creating chemically favorable conditions to particles inception between the liquid interface ($\Phi \to \infty$) and the flame front ($\Phi \simeq 1$), and (ii) the competition between convective transport due to evaporation (Stefan flow), and the thermophoretic transport affecting solid particles. They act in opposite directions in the inner part of the flame: under constant-pressure and radial symmetry hypotheses, the Stefan velocity can be obtained through the continuity equation:

$$v_{\text{Stefan}} = \frac{1}{\rho_G} \frac{\dot{m}_{ev}}{4\pi r^2} \tag{15}$$

where $\dot{m}_{ev}$ is the droplet evaporation rate. Thermophoretic velocity was defined in Eq. (13). Figure 9 shows the predicted velocity profiles at different time steps for a sample droplet. Stefan velocity (Fig. 9a) undergoes an initial increase because of the sudden drop of density (Fig. 10), on turn due to the steep increase in temperature and decrease in molecular weight (Fig. 8). Afterwards, the effect of distance ($\propto \frac{1}{r^2}$) prevails, and v_{Stefan} decreases asymptotically to zero. On the other side, the behavior of the thermophoretic velocity (Fig. 9b) is more complex and non-linear, because of the combination of (i) viscosity (Fig. 10), (ii) density and (iii) temperature. The progressive decrease results in a non-monotonic trend, and the minimum is located approximately halfway between the interface and the flame front. The net result of this competition is the establishment of two equilibrium points (Fig. 9c), as already noticed in previous works, which adopted a more simplified approach [30,37]. Looking at the sign of the derivative, the inner one can be recognized as stable ($dv/dr < 0$), while the outer one is unstable ($dv/dr > 0$). As a result, the nucleated soot particles are pushed towards the inner equilibrium point, where the residence times are maximum and they can find kinetically favorable conditions (high T and Φ) for their growth and accumulation. A deeper insight in the kinetic evolution of the system is provided in Fig. 11a. Here, the evolution of representative reaction rates of the different classes, indicated in detail in Table 3, are reported. It is possible to observe that the inception of soot particles occurs close to the flame front, where the concentration of precursors is
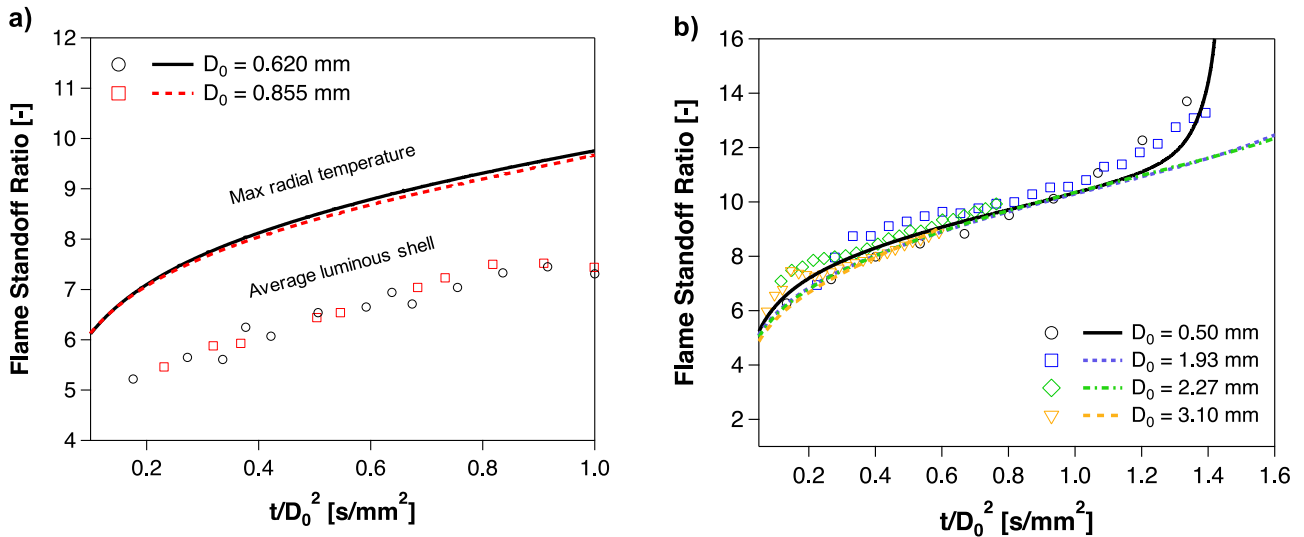
Fig. 7. FSR evolution for different initial diameters and set of experiments: comparison between experimental data and numerical predictions. Experimental data from (a) [13] and (b) [21]. (For interpretation of the references to color in this figure, the reader is referred to the web version of this article.)
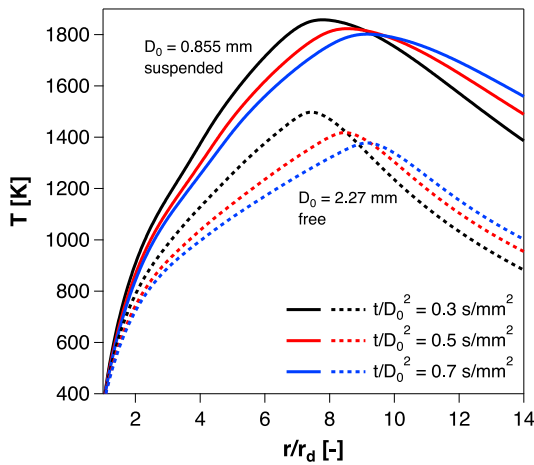

Fig. 8. Comparison between predicted gas-phase temperature of a sub-millimetric [13] and a super-millimetric [21] droplet.
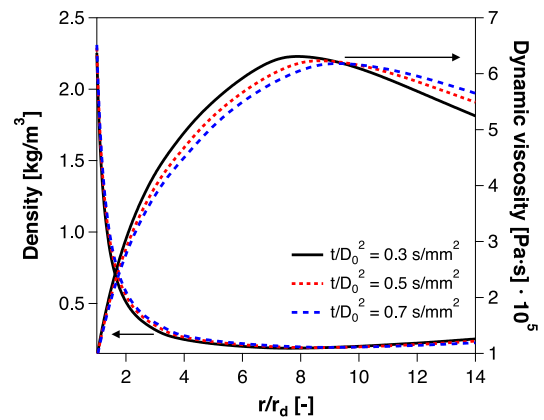

Fig. 10. Predicted density and viscosity at different time steps for the droplet with $D_0 = 0.855$ mm [13].

maximum because of the higher residence times, and the higher temperatures favor the kinetics of nucleation. Following inception, the HACA (Hydrogen-Abstraction / Acetylene-Addition) mechanism occurs, whose peak is located farther from the flame front, where acetylene concentration is also higher (i.e. in the richer region). In the same area, surface growth and coalescence occur, which only involve solid particles, and then feel the effect of thermophoresis. Later, aggregation further contributes to the growth in size, and it can be seen that (i) it occurs closer to the interface, since it involves larger particles, and (ii) it covers a broader region, since the maximum concentration of aggregates is located far from the reaction zone. As it can be seen from soot volume fraction in Fig. 11b,
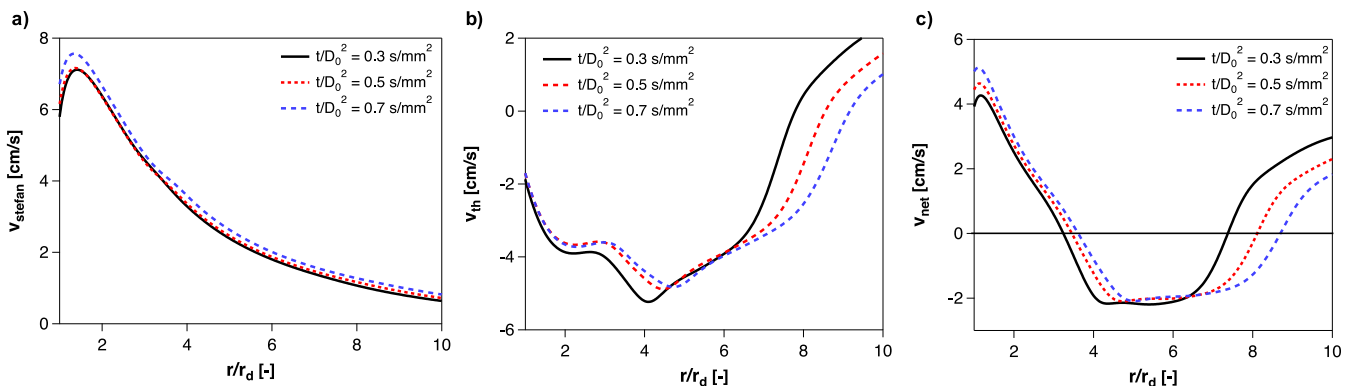

Fig. 9. Predicted velocity profiles at different time steps for the droplet with $D_0 = 0.855$ mm [13]. (a) Stefan velocity. (b) Thermophoretic velocity. (c) Net velocity.
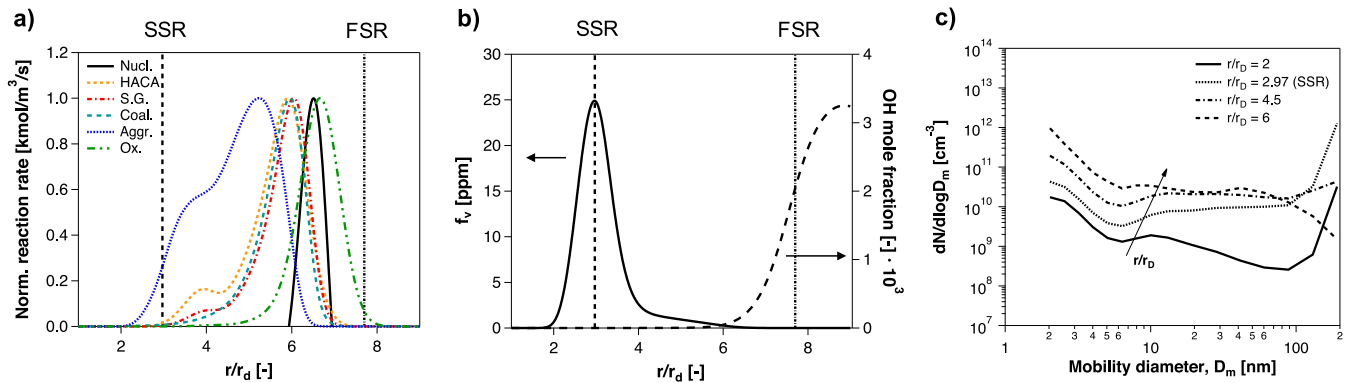
Fig. 11. Dynamics of soot formation, growth and oxidation between droplet interface and flame front. (a) Normalized kinetic rates of sample reactions (see Table 3); (b) Comparison between soot volume fraction and OH profiles; (c) Radial evolution of soot PSDF. $D_0 = 0.855$ mm; $t/D_0^2 = 0.3\,s/mm^2$.
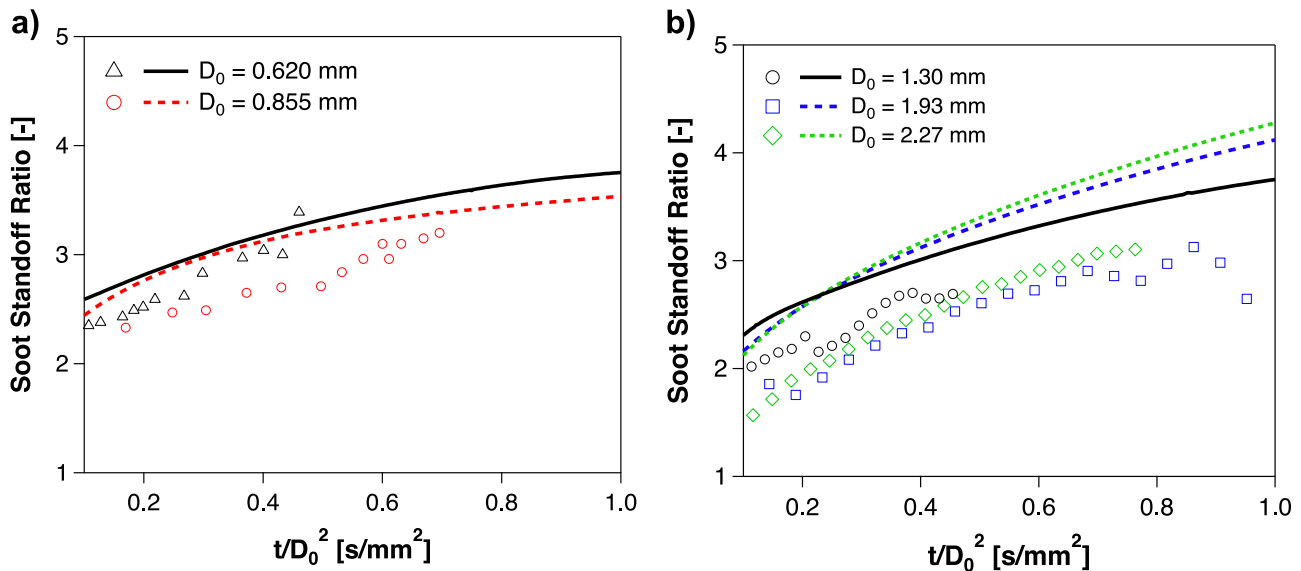

Fig. 12. SSR evolution for different initial diameters and set of experiments: comparison between experimental data and model predictions. (a) Small diameters (ground-based droplets) [13]. (b) Large diameters (free droplets) [21].

Table 3
Representative reaction rates of the major classes involved in soot dynamics. $D_0 = 0.855$ mm; $t/D_0^2 = 0.3\,s/mm^2$. The full list of reaction classes is available in the work by Saggese et al. [60].

Class	Abbreviation	Representative reaction	Max radial value [$kmol/m^3 s$]
Nucleation	Nucl.	reactants → BIN5	1.2e−7
Acetylene addition	HACA	$C_2H_2 + BIN_i· →$ products	2.4e−5
Surface growth	S.G.	$BIN_i + BIN_j →$ products $i < 5, j \geq 5$	3.4e−6
Coalescence	Coal.	$BIN_i + BIN_j →$ products $5 \leq i, j < 13$	6.4e−8
Aggregation	Aggr.	$BIN_i + BIN_j →$ products $i, j \geq 13$	6.0e−9
Oxidation	Ox.	$BIN_i + OH →$ products $BIN_i· + OH →$ products	2.2e−4

the actual soot shell is located in a non-reactive region, where soot is only transported because of thermophoresis, and temperatures are too low (cfr. Fig. 8) to allow any significant reactivity (with the exception of aggregation). Finally, as expected, oxidation takes place closer to the flame front than other classes: as shown in Fig. 11b, the location of its peak depends on both the availability of the oxydril radical and the residual presence of soot parti-

cles. The estimation of the PSDF (Fig. 11c) confirms that, while in proximity of the flame front the particle distribution is comparable to what usually observed in flames [7,59], an accumulation of heavier particles is observed when moving closer to the soot shell, where the thermophoretic transport moves the aggregates away from the reactive zone towards the stable equilibrium point. The rise in the number of particles with the largest diameters in correspondence of the soot shell is actually due to the finite number of discrete sections used to model the aerosol phase, which prevents the further growth of particles larger than 200 nm, and then foster their accumulation. Although it is outside the scope of this work, it is worth mentioning that the extension of the kinetic model to account for larger diameters is matter of current research. This will allow to analyse the sensitivity of the particle-size distribution to the upper limit of the particles dimension described in the kinetic mechanism.

The soot shell is thus the macroscopic result of the balance between thermophoretic and Stefan flow and is measured in terms of relative distance from the droplet center (Soot Standoff Ratio – SSR). Experimentally, the SSR is usually evaluated via direct photographs observations, while in numerical terms, SSR is estimated through the normalized radial coordinate with the maximum f_v. Figure 12 shows the evolution of SSR as a function of
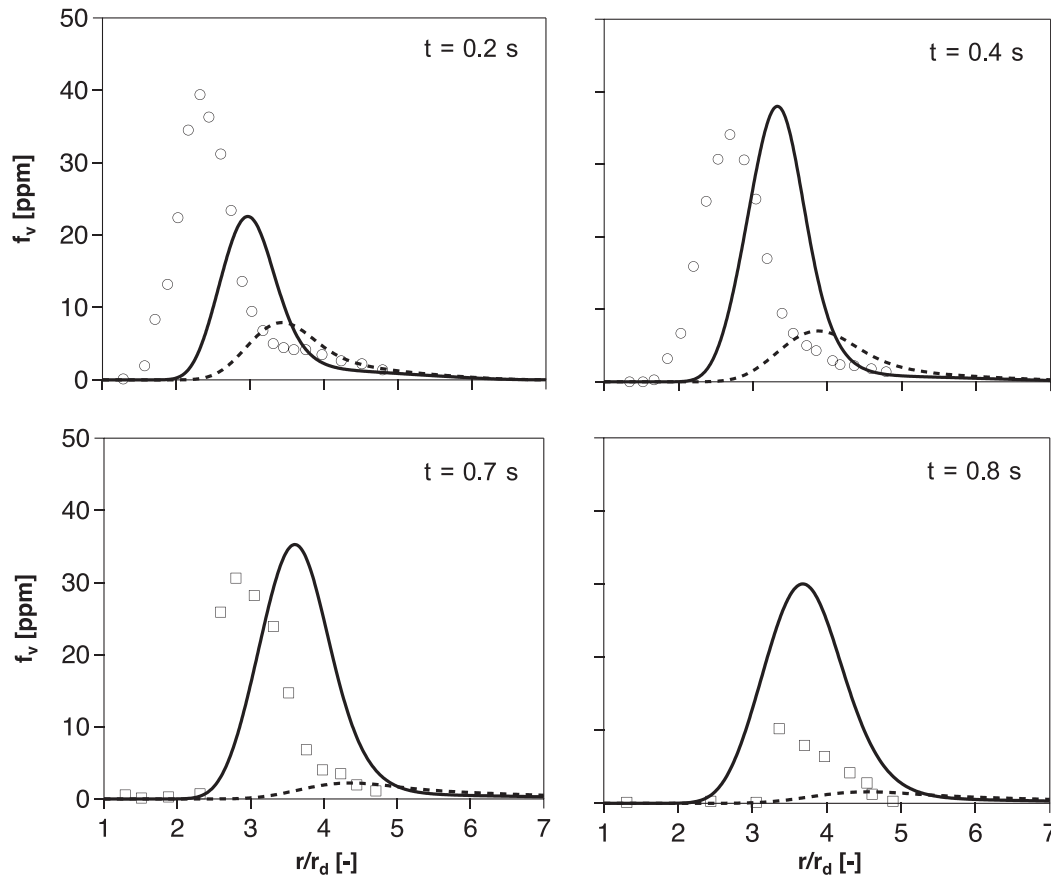
Fig. 13. Predicted vs experimental [16] soot volume fraction profiles at different time steps. Solid lines: results with $V_{th,r} = 0.654$ (Beresnev and Chernyak [54] with $\alpha_T = 0.54$). Dashed lines: results with $V_{th,r} = 0.538$ (Waldmann and Schmitt [48]). $D_0 = 0.84$ mm.

normalized time for two sets of experiments. Comparable trends are observed in both ground-based and outer-space measurements, although an overestimation of about half diameter is generally observed. For smaller D_0, SSR is initially slightly higher because the evaporation rate is stronger (Fig. 6b), and so is Stefan velocity. A flatter evolution over time can be observed in sub-millimetric droplets, which follows the progressive slight departure of the thermophoretic velocity profile (Fig. 9b), on turn due to FSR slightly moving away from the surface (Fig. 7a). Conversely, for larger droplets the evaporation rate is smaller, and radiative losses progressively decrease the flame temperature (Fig. 8), causing the weakening of the thermophoretic transport. Figure 12b shows that SSR is initially higher for the smallest droplet ($D_0 = 1.30$ mm), as a result of the higher evaporation rate. Later, the evolution of SSR in the larger ones follows a steeper trend, in parallel with the decrease of the flame temperature.

Additional details of these dynamics are provided by the variation in soot volume fraction over time. Figure 13 shows the results obtained for a sub-millimetric ($D_0 = 0.84$ mm) droplet, which had been experimentally investigated by Lee et al. [16]. These trends are coherent with that observed so far, i.e. the distribution shifted outwards of about half diameter, whereas the quantitative predictions of f_v are in reasonable agreement with measurements. Such behavior proved extremely sensitive to the thermophoretic law: by adopting $V_{th,r} = 0.538$, i.e. by supposing $\alpha_T = 1$, SSR is further overpredicted (1/2 diameters more), while the maximum f_v is four times lower than what obtained by introducing incomplete thermal accommodation. Obtaining further improvements in this direction is not straightforward: the location and the intensity of the volume fraction profile depends on a significant number of fac-

tors and related submodels. Beyond the description of the thermophoretic effect, it is worth mentioning: (i) the inclusion of diffusiophoresis and photophoresis; (ii) the influence of radiation and (iii) the uncertainty related to the kinetic mechanism in all of its constituting classes.

As concerns the impact of radiation, it was already seen that the coupled use of a P1/WSGG approach underestimates the evaporation rate for super-millimetric droplets (Fig. 6b), bringing to an earlier extinction (Fig. 6c). This has an impact on the flame temperature (Fig. 8), and consequently on the kinetic rates of soot formation. Figure 14 shows the predictions of f_v for a relatively large droplet ($D_0 = 2.90$ mm), already studied by Manzello et al. [17]. It is shown that, although the initial increase is well caught and a reasonable agreement with SSR is observed (a slight overprediction is again obtained), the peak of volume fraction is underestimated. The maximum f_v starts decreasing at $t = 0.7$ s, i.e. at the same time as the experimental measurements, whereas the predicted decrease rate is slower than the experimental. The correction of the radiative contribution by a factor 0.75, in the wake of what previously done (Fig. 6c), provides results more in line with measurements. On the other side, the correction of the radiation model does not have a significant influence on SSR or the decrease rate. A peak-shoulder shape is also suggested by the experimental data but not reproduced experimentally; yet, considering the irregular profile in the soot tail, as well as the reported uncertainty in measurements (25%), it cannot be considered as relevant from a modeling standpoint.

Finally, sensitivity analysis was carried out using brute-force method, in order to define the impact of the different submodels constituting the kinetic mechanism on the obtained results: the ki-
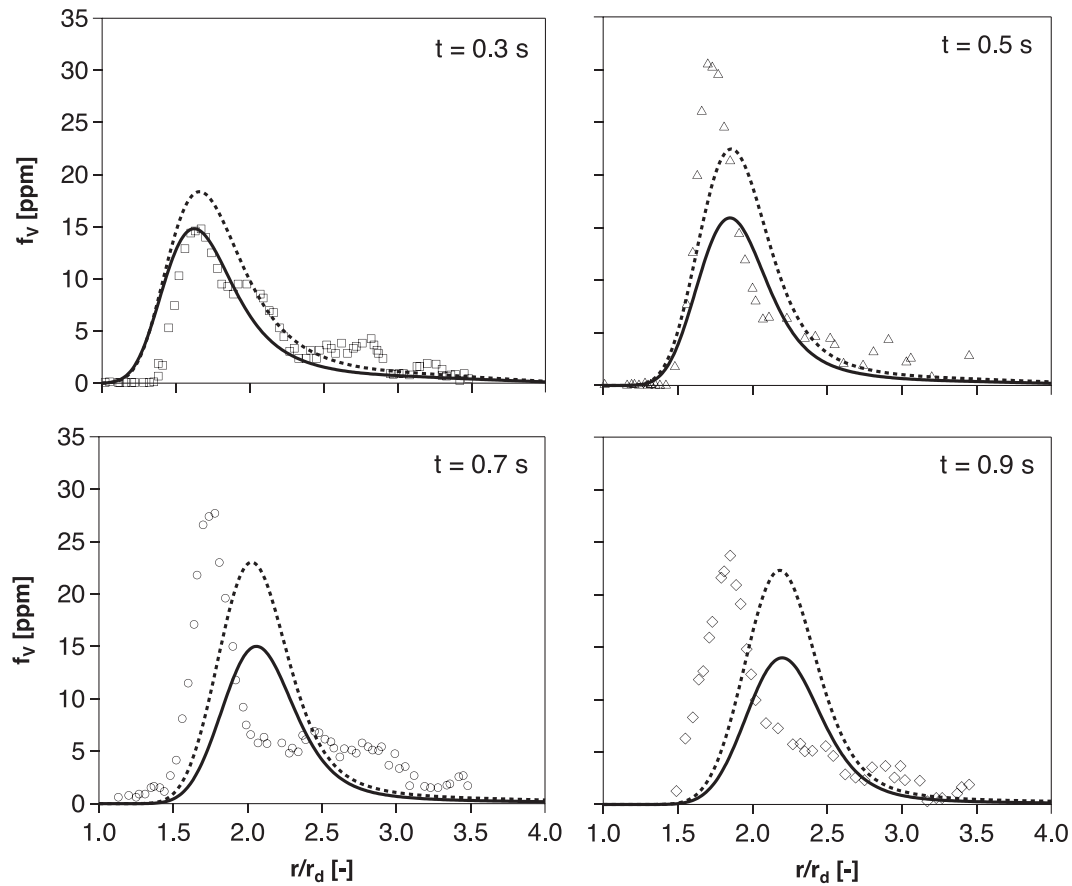
Fig. 14. Predicted vs experimental [17] soot volume fraction profiles at different time steps. Solid lines: results with standard P1/WSGG radiation model. Dashed lines: results with P1/WSGG radiation model, corrected by a factor 0.75 (cfr. Fig. 6c). $D_0 = 2.90$ mm.
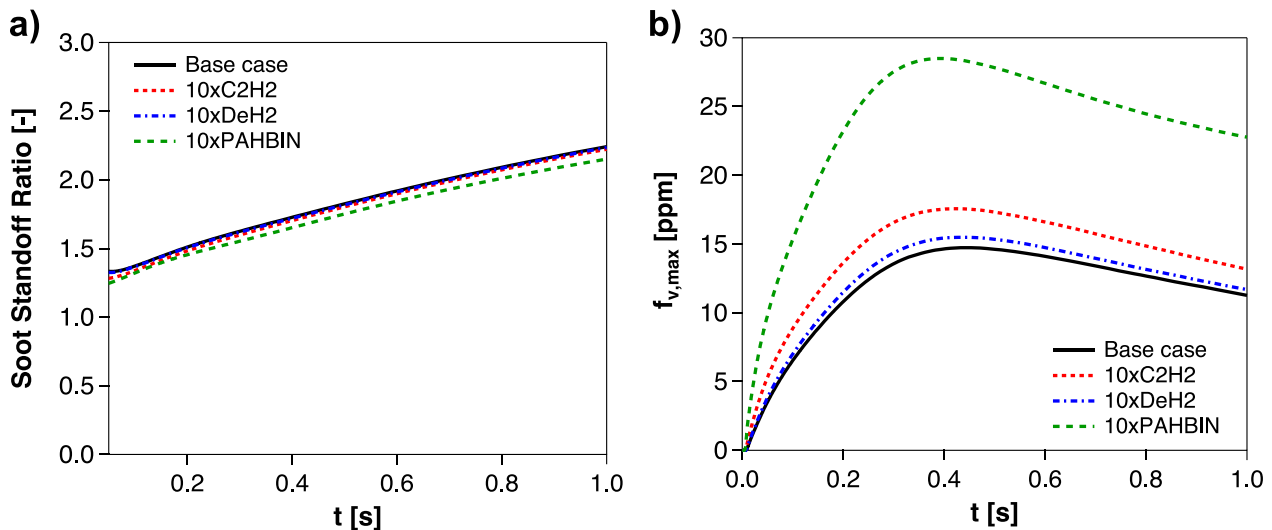

Fig. 15. Sensitivity of (a) SSR and (b) maximum radial f_v to the kinetic rates of the different reaction classes. $D_0 = 2.90$ mm.

netic rates of different reaction classes were increased by a factor 10, and the macroscopic results in terms of SSR and f_v were analysed. The related sensitivities to acetylene addition, dehydrogenation and PAH addition were investigated considering the droplet already simulated in Fig. 14, and are presented in Fig. 15 for $D_0 =$ 2.90 mm. The evolution of SSR is not affected by such increase in

a significant way, with the exception of the PAH addition to BINs. In this case, the soot shell is closer to the surface, although still larger than the experimental value. On the other side, the change in soot volume fraction is much more evident, as the obtained profiles are a factor ~ 2 larger over time. These results substantially confirm the analysis carried out by Saggese et al. [60] on a burner-

stabilized premixed flame, which identified C_2H_2- and especially PAH-addition as the reaction classes having the largest impact on volume fraction. Yet, PAH-addition alone is not able to explain the residual deviations between model and experiments, since the location of the soot shell is still overpredicted, in spite of a good agreement with f_v measurements.

5. Conclusions

In this work, the dynamics of soot formation, growth and oxidation from the combustion of isolated droplets in microgravity conditions was investigated. For the first time (to the authors' knowledge), a detailed, heterogeneous kinetic model was used, to get a qualitative and quantitative understanding of the underlying physics. The use of a discrete sectional approach to describe the solid phase, and of reaction classes in analogy with what done with the gas phase, allowed to get an insight on the fundamental processes at stake. A P1/WSGG radiation model was implemented in order to have a comprehensive description of radiation (including soot), while a size-independent law, accounting for incomplete thermal accommodation, was used to describe the thermophoretic effect. A skeletal reduction on the detailed mechanism was carried out upstream to accelerate simulations.

Using n-heptane as test fuel, the model was applied to examine an extended range of initial diameters ($D_0 = 0.50 - 3.87$ mm), to replicate the experimental campaigns carried out in the latest decades in drop towers and outer space. A good agreement with experimental data was observed in terms of flame development, as the flame temperature and standoff ratio satisfactorily matched the available measurements. A slightly higher detachment of the flame was observed for smaller diameters, coherently with the higher temperatures involved due to a limited impact of radiation. For larger (super-millimetric) droplets, though, the model proved extremely sensitive to radiation, and the use of a P1/WSGG model resulted in the underestimation of evaporation rates and extinction times, regardless of the procedure used to estimate the coefficients of the equivalent gray gases. To overcome this issue, either an empirical correction can be adopted for the largest droplets, or alternative models must be sought [83].

The model also allowed to locate and quantify the different steps of soot evolution, which were found to occur in the region between Flame and Soot Standoff Ratio, where the combination of Stefan and thermophoretic effects results in a flux directed inwards. A further effect of the inward flux consisted in the change of the shape of the Particle Size Distribution Function, which in proximity of SSR showed a modification with respect to what observed in premixed flames [7,60], due to the accumulation of heavy particles. To this regard, PSDF predictions felt the effect of the upper threshold in size of the discrete sectional model, which is set to a diameter of 200 nm so far. Indeed, the uniquely high residence times of the this system result in the formation of unusually large aggregates, as also observed experimentally [49]. The forthcoming extension of the discrete sectional model to larger diameters will be able to include also this aspect.

The evolution of the soot volume fraction profile resulted then from the combination of thermophoretic flux and radiation, with a significant sensitivity to both of them. Thermophoresis was found to affect both the amount of produced soot, as well as the location of the Standoff Ratio. The use of the formulation by Waldmann and Schmitt [48] significantly underestimated the amounts of produced soot, while the inclusion of incomplete thermal accommodation provided much better predictions, overestimating the position of the soot shell by about half a diameter. On the other side, the overestimation of radiative heat loss for larger diameters affected soot production in the same direction because of the reduced kinetic rates, and its correction resulted in an improvement of predictions.

References

[1] A. Tewarson, Combustion efficiency and its radiative component, Fire Safety J. 39 (2) (2004) 131–141.

[2] J. Hansen, L. Nazarenko, Soot climate forcing via snow and ice albedos, Proc. Nat. Acad. Sci. USA 101 (2) (2004) 423–428.

[3] T.C. Bond, S.J. Doherty, D. Fahey, P. Forster, T. Berntsen, B. DeAngelo, M. Flanner, S. Ghan, B. Kärcher, D. Koch, et al., Bounding the role of black carbon in the climate system: a scientific assessment, J. Geophys. Res. Atmos. 118 (11) (2013) 5380–5552.

[4] I.M. Kennedy, The health effects of combustion-generated aerosols, Proc. Combust. Inst. 31 (2) (2007) 2757–2770.

[5] N.A.H. Janssen, W. Joint, Health effects of black carbon, World Health Organization, Regional Office for Europe, Copenhagen, 2012.

[6] M. Shiraiwa, K. Selzle, U. Pöschl, Hazardous components and health effects of atmospheric aerosol particles: reactive oxygen species, soot, polycyclic aromatic compounds and allergenic proteins, Free Radic. Res. 46 (8) (2012) 927–939.

[7] H. Wang, Formation of nascent soot and other condensed-phase materials in flames, Proc. Combust. Inst. 33 (1) (2011) 41–67.

[8] A.J. Marchese, F.L. Dryer, V. Nayagam, Numerical modeling of isolated n-alkane droplet flames: initial comparisons with ground and space-based microgravity experiments, Combust. Flame 116 (3) (1999) 432–459.

[9] C.T. Avedisian, Recent advances in soot formation from spherical droplet flames at atmospheric pressure, J. Propul. Power 16 (4) (2000) 628–635.

[10] S. Kumar, A. Ray, S. Kale, A soot model for transient, spherically symmetric n-heptane droplet combustion, Combust. Sci. Technol. 174 (9) (2002) 67–102.

[11] D.L. Dietrich, V. Nayagam, M.C. Hicks, P.V. Ferkul, F.L. Dryer, T. Farouk, B.D. Shaw, H.K. Suh, M.Y. Choi, Y.C. Liu, et al., Droplet combustion experiments aboard the international space station, Microgr. Sci. Technol. 26 (2) (2014) 65–76.

[12] B. Shaw, F. Dryer, F. Williams, J. Haggard, Sooting and disruption in spherically symmetrical combustion of decane droplets in air, Acta Astronaut. 17 (11–12) (1988) 1195–1202.

[13] G. Jackson, C. Avedisian, The effect of initial diameter in spherically symmetric droplet combustion of sooting fuels, Royal Society of London A: Mathematical, Physical and Engineering Sciences, 446, The Royal Society (1994), pp. 255–276.

[14] M. Mikami, M. Niwa, H. Kato, J. Sato, M. Kono, Clarification of the flame structure of droplet burning based on temperature measurement in microgravity, Symp. (Int.) Combust., 25, Elsevier (1994), pp. 439–446.

[15] M.Y. Choi, K.-O. Lee, Investigation of sooting in microgravity droplet combustion, Symp. (Int.) Combust., 26, Elsevier (1996), pp. 1243–1249.

[16] K.-O. Lee, S.L. Manzello, M.Y. Choi, The effects of initial diameter on sooting and burning behavior of isolated droplets under microgravity conditions, Combust. Sci. Technol. 132 (1–6) (1998) 139–156.

[17] S.L. Manzello, M.Y. Choi, A. Kazakov, F.L. Dryer, R. Dobashi, T. Hirano, The burning of large n-heptane droplets in microgravity, Proc. Combust. Inst. 28 (1) (2000) 1079–1086.

[18] M. Kashif, P. Guibert, J. Bonnety, G. Legros, Sooting tendencies of primary reference fuels in atmospheric Laminar diffusion flames burning into vitiated air, Combust. Flame 161 (6) (2014) 1575–1586.

[19] M. Kashif, J. Bonnety, A. Matynia, P. Da Costa, G. Legros, Sooting propensities of some gasoline surrogate fuels: combined effects of fuel blending and air vitiation, Combust. Flame 162 (5) (2015) 1840–1847.

[20] V. Nayagam, D.L. Dietrich, M.C. Hicks, F.A. Williams, Cool-flame extinction during n-alkane droplet combustion in microgravity, Combust. Flame 162 (5) (2015) 2140–2147.

[21] Y.C. Liu, Y. Xu, M.C. Hicks, C.T. Avedisian, Comprehensive study of initial diameter effects and other observations on convection-free droplet combustion in the standard atmosphere for n-heptane, n-octane, and n-decane, Combust. Flame 171 (2016) 27–41.

[22] V. Nayagam, D.L. Dietrich, P.V. Ferkul, M.C. Hicks, F.A. Williams, Can cool flames support Quasi-steady alkane droplet burning? Combust. Flame 159 (12) (2012) 3583–3588.

[23] C. Law, Recent advances in droplet vaporization and combustion, Progress Energy Combust. Sci. 8 (3) (1982) 171–201.

[24] G. Faeth, Evaporation and combustion of sprays, Progress Energy Combust. Sci. 9 (1) (1983) 1–76.

[25] A. Kazakov, J. Conley, F.L. Dryer, Detailed modeling of an isolated, ethanol droplet combustion under microgravity conditions, Combust. Flame 134 (4) (2003) 301–314.

[26] T. Farouk, Y. Liu, A. Savas, C. Avedisian, F. Dryer, Sub-millimeter sized methyl butanoate droplet combustion: microgravity experiments and detailed numerical modeling, Proc. Combust. Inst. 34 (1) (2013) 1609–1616.

[27] K.-C. Chang, J.-S. Shier, Theoretical investigation of transient droplet combustion by considering flame radiation, Int. J. Heat Mass Transf. 38 (14) (1995) 2611–2621.

[28] S.W. Baek, J.H. Park, C.E. Choi, Investigation of droplet combustion with nongray gas radiation effects, Combust. Sci. Technol. 142 (1–6) (1999) 55–79.

[29] J. Moss, C. Stewart, K. Syed, Flowfield modelling of soot formation at elevated pressure, Symp. (Int.) Combust., 22, Elsevier (1989), pp. 413–423.

[30] G. Jackson, C. Avedisian, Modeling of spherically symmetric droplet flames including complex chemistry: effect of water addition on n-heptane droplet combustion, Combust. Sci. Technol. 115 (1–3) (1996) 125–149.

[31] R. Stauch, S. Lipp, U. Maas, Detailed numerical simulations of the autoignition of single n-heptane droplets in air, Combust. flame 145 (3) (2006) 533–542.

[32] A. Cuoci, M. Mehl, G. Buzzi-Ferraris, T. Faravelli, D. Manca, E. Ranzi, Autoignition and burning rates of fuel droplets under microgravity, Combust. Flame 143 (3) (2005) 211–226.

[33] A. Cuoci, A. Frassoldati, T. Faravelli, E. Ranzi, Numerical modeling of auto-ignition of isolated fuel droplets in microgravity, Proc. Combust. Inst. 35 (2) (2015) 1621–1627.

[34] C.L. Yaws, The Yaws handbook of physical properties for hydrocarbons and chemicals, Gulf Professional Publishing, 2015.

[35] P. Keller, A. Bader, C. Hasse, The influence of intra-droplet heat and mass transfer limitations in evaporation of binary hydrocarbon mixtures, Int. J. Heat Mass Transf. 67 (2013) 1191–1207.

[36] A. Perea, P. Garcia-Ybarra, J. Castillo, Soot diffusive transport effects affecting soot shell formation in droplet combustion, Mediterranean Combustion Symposium (1999), pp. 275–285.

[37] G. Ben-Dor, T. Elperin, B. Krasovit, Effect of thermo–and diffusiophoretic forces on the motion of flame-generated particles in the neighbourhood of burning droplets in microgravity conditions, Royal Society of London A: Mathematical, Physical and Engineering Sciences, 459, The Royal Society (2003), pp. 677–703.

[38] A. Cuoci, A.E. Saufi, A. Frassoldati, D.L. Dietrich, F.A. Williams, T. Faravelli, Flame extinction and low-temperature combustion of isolated fuel droplets of n-alkanes, Proc. Combust. Inst. 36 (2) (2017) 2531–2539.

[39] M.F. Modest, Radiative heat transfer, Academic Press, 2013.

[40] M.F. Modest, The weighted-sum-of-gray-gases model for arbitrary solution methods in radiative transfer, J. Heat Transf. 113 (3) (1991) 650–656.

[41] T. Smith, Z. Shen, J. Friedman, Evaluation of coefficients for the weighted sum of gray gases model, J. Heat Transf. 104 (4) (1982) 602–608.

[42] C. Yin, Refined weighted sum of gray gases model for air-fuel combustion and its impacts, Energy Fuels 27 (10) (2013) 6287–6294.

[43] T.F. Smith, A.M. Al-Turki, K.-H. Byun, T.K. Kim, Radiative and conductive transfer for a gas/soot mixture between diffuse parallel plates, J. Thermophys. Heat Transf. 1 (1) (1987) 50–55.

[44] F. Cassol, R. Brittes, F.H. França, O.A. Ezekoye, Application of the weighted–sum-of-gray-gases model for media composed of arbitrary concentrations of H_2O, CO_2 and soot, Int. J. Heat Mass Transf. 79 (2014) 796–806.

[45] G. Jackson, C. Avedisian, J. Yang, Observations of soot during droplet combustion at low gravity: heptane and heptane/monochloroalkane mixtures, Int. J. Heat Mass Transf. 35 (8) (1992) 2017–2033.

[46] G. Santachiara, F. Prodi, C. Cornetti, Experimental measurements on thermophoresis in the transition region, J. Aerosol Sci. 33 (5) (2002) 769–780.

[47] B. Sagot, Thermophoresis for spherical particles, J. Aerosol Sci. 65 (2013) 10–20.

[48] L. Waldmann, K. Schmitt, Thermophoresis and diffusiophoresis of aerosols, Aerosol Sci. 137 (1966).

[49] H. Ono, R. Dobashi, T. Sakuraya, Thermophoretic velocity measurements of soot particles under a microgravity condition, Proc. Combust. Inst. 29 (2) (2002) 2375–2382.

[50] D. Rosner, D. Mackowski, P. Garcia-Ybarra, Size-and structure-Insensitivity of the thermophoretic transport of aggregated "soot" particles in gases, Combust. Sci. Technol. 80 (1–3) (1991) 87–101.

[51] L. Talbot, R. Cheng, R. Schefer, D. Willis, Thermophoresis of particles in a heated boundary layer, J. Fluid Mech. 101 (04) (1980) 737–758.

[52] D.R. Snelling, F. Liu, G.J. Smallwood, Ö.L. Gülder, Determination of the soot absorption function and thermal accommodation coefficient using low-fluence LII in a Laminar coflow ethylene diffusion flame, Combust. Flame 136 (1) (2004) 180–190.

[53] S.L. Manzello, M.Y. Choi, Morphology of soot collected in microgravity droplet flames, Int. J. Heat Mass Transf. 45 (5) (2002) 1109–1116.

[54] S. Beresnev, V. Chernyak, Thermophoresis of a spherical particle in a rarefied gas: numerical analysis based on the model kinetic equations, Phys. Fluids (1994-present) 7 (7) (1995) 1743–1756.

[55] B. Sagot, G. Antonini, F. Buron, Annular flow configuration with high deposition efficiency for the experimental determination of thermophoretic diffusion coefficients, J. Aerosol Sci. 40 (12) (2009) 1030–1049.

[56] E. Ranzi, A. Frassoldati, R. Grana, A. Cuoci, T. Faravelli, A. Kelley, C. Law, Hierarchical and comparative kinetic modeling of Laminar flame speeds of hydrocarbon and oxygenated fuels, Progress Energy Combust. Sci. 38 (4) (2012) 468–501.

[57] E. Ranzi, P. Gaffuri, T. Faravelli, P. Dagaut, A wide-range modeling study of n-heptane oxidation, Combust. Flame 103 (1) (1995) 91–106.

[58] S. Humer, A. Frassoldati, S. Granata, T. Faravelli, E. Ranzi, R. Seiser, K. Seshadri, Experimental and kinetic modeling study of combustion of JP-8, its surrogates and reference components in Laminar nonpremixed flows, Proc. Combust. Inst. 31 (1) (2007) 393–400.

[59] C. Saggese, A. Frassoldati, A. Cuoci, T. Faravelli, E. Ranzi, A wide range kinetic modeling study of pyrolysis and oxidation of benzene, Combust. Flame 160 (7) (2013) 1168–1190.

[60] C. Saggese, S. Ferrario, J. Camacho, A. Cuoci, A. Frassoldati, E. Ranzi, H. Wang, T. Faravelli, Kinetic modeling of particle size distribution of soot in a premixed burner-stabilized stagnation ethylene flame, Combust. Flame 162 (9) (2015) 3356–3369.

[61] A.L. Lafleur, K. Taghizadeh, J.B. Howard, J.F. Anacleto, M.A. Quilliam, Characterization of flame-generated C10 to C160 polycyclic aromatic hydrocarbons by atmospheric-pressure chemical ionization mass spectrometry with liquid introduction via heated nebulizer interface, J. Am. Soc. Mass Spectrom. 7 (3) (1996) 276–286.

[62] L. Sgro, A. De Filippo, G. Lanzuolo, A. D'Alessio, Characterization of nanoparticles of organic carbon (NOC) produced in rich premixed flames by differential mobility analysis, Proc. Combust. Inst. 31 (1) (2007) 631–638.

[63] L. Sgro, A. Barone, M. Commodo, A. D'Alessio, A. De Filippo, G. Lanzuolo, P. Minutolo, Measurement of nanoparticles of organic carbon in non-sooting flame conditions, Proc. Combust. Inst. 32 (1) (2009) 689–696.

[64] A. Abid, E. Tolmachoff, D. Phares, H. Wang, Y. Liu, A. Laskin, Size distribution and morphology of nascent soot in premixed ethylene flames with and without benzene doping, Proc. Combust. Inst. 32 (1) (2009) 681–688.

[65] H. Bladh, N.-E. Olofsson, T. Mouton, J. Simonsson, X. Mercier, A. Faccinetto, P.-E. Bengtsson, P. Desgroux, Probing the smallest soot particles in low-sooting premixed flames using laser-induced incandescence, Proc. Combust. Inst. 35 (2) (2015) 1843–1850.

[66] B. Zhao, K. Uchikawa, H. Wang, A comparative study of nanoparticles in premixed flames by scanning mobility particle sizer, small angle neutron scattering, and transmission electron microscopy, Proc. Combust. Inst. 31 (1) (2007) 851–860.

[67] M. Schenk, S. Lieb, H. Vieker, A. Beyer, A. Gölzhäuser, H. Wang, K. Kohse-Höinghaus, Morphology of nascent soot in ethylene flames, Proc. Combust. Inst. 35 (2) (2015) 1879–1886.

[68] M.M. Maricq, Coagulation dynamics of fractal-like soot aggregates, J. Aerosol Sci. 38 (2) (2007) 141–156.

[69] L. Brown, N. Collings, R. Harrison, A. Maynard, R. Maynard, Ultrafine particles in the atmosphere, Imperial College Press, 2003.

[70] X. Zheng, T. Lu, C. Law, Experimental counterflow ignition temperatures and reaction mechanisms of 1, 3-butadiene, Proc. Combust. Inst. 31 (1) (2007) 367–375.

[71] K.E. Niemeyer, C.-J. Sung, M.P. Raju, Skeletal mechanism generation for surrogate fuels using directed relation graph with error propagation and sensitivity analysis, Combust. Flame 157 (9) (2010) 1760–1770.

[72] F. Xu, A. El-Leathy, C. Kim, G. Faeth, Soot surface oxidation in hydrocarbon/air diffusion flames at atmospheric pressure, Combust. flame 132 (1) (2003) 43–57.

[73] A. Stagni, A. Frassoldati, A. Cuoci, T. Faravelli, E. Ranzi, Skeletal mechanism reduction through species-targeted sensitivity analysis, Combust. Flame 163 (2016) 382–393.

[74] P. Berta, S.K. Aggarwal, I.K. Puri, An experimental and numerical investigation of n-heptane/air counterflow partially premixed flames and emission of NO x and PAH species, Combust. Flame 145 (4) (2006) 740–764.

[75] A.E. Bakali, J.-L. Delfau, C. Vovelle, Experimental study of 1 atmosphere, rich, premixed n-heptane and ISO-octane flames, Combust. Sci. Technol. 140 (1–6) (1998) 69–91.

[76] F. İnal, S.M. Senkan, Effects of equivalence ratio on species and soot concentrations in premixed n-heptane flames, Combust. Flame 131 (1) (2002) 16–28.

[77] A. D'Anna, M. Alfe, B. Apicella, A. Tregrossi, A. Ciajolo, Effect of fuel/air ratio and aromaticity on sooting behavior of premixed heptane flames, Energy Fuels 21 (5) (2007) 2655–2662.

[78] B. Hu, B. Yang, U.O. Koylu, Soot measurements at the axis of an ethylene/air non-premixed turbulent jet flame, Combust. Flame 134 (1) (2003) 93–106.

[79] A. Cuoci, A. Frassoldati, T. Faravelli, E. Ranzi, A computational tool for the detailed kinetic modeling of Laminar flames: application to C_2H_4/CH_4 coflow flames, Combust. Flame 160 (5) (2013) 870–886.

[80] G. Xu, M. Ikegami, S. Honma, K. Ikeda, D.L. Dietrich, P.M. Struk, Interactive influences of convective flow and initial droplet diameter on isolated droplet burning rate, Int. J. Heat Mass Transf. 47 (8) (2004) 2029–2035.

[81] A.J. Marchese, F.L. Dryer, The effect of non-luminous thermal radiation in microgravity droplet combustion, Combust. Sci. Technol. 124 (1–6) (1997) 371–402.

[82] T.I. Farouk, F.L. Dryer, Isolated n-heptane droplet combustion in microgravity:"cool flames"–two-stage combustion, Combust. Flame 161 (2) (2014) 565–581.

[83] T. Farouk, D. Dietrich, F. Alam, F. Dryer, Isolated n-decane droplet combustion—dual stage and single stage transition to "cool flame" droplet burning, Proc. Combust. Inst. 36 (2) (2017) 2523–2530.

[84] C.A. Echavarria, I.C. Jaramillo, A.F. Sarofim, J.S. Lighty, Studies of soot oxidation and fragmentation in a two-stage burner under fuel-lean and fuel-rich conditions, Proc. Combust. Inst. 33 (1) (2011) 659–666.